An inverse optimization strategy to determine single crystal mechanical behavior from polycrystal tests: Application to AZ31 Mg alloy

V. Herrera-Solaz , J. LLorca , E. Dogan , I. Karaman , J. Segurado

A B S T R A C T

An inverse optimization strategy was developed to determine the single crystal properties from experimental results of the mechanical behavior of polycrystals. The polycrystal behavior was obtained by means of the finite element simulation of a representative volume element of the microstructure in which the dominant slip and twinning systems were included in the constitutive equation of each grain. The inverse problem was solved by means of the Levenberg–Marquardt method, which provided an excellent fit to the experimental results. The iterative optimization process followed a hierarchical scheme in which simple representative volume elements were initially used, followed by more realistic ones to reach the final optimum solution, leading to important reductions in computer time. The new strategy was applied to identify the initial and saturation critical resolved shear stresses and the hardening modulus of the active slip systems and extension twinning in a textured AZ31 Mg alloy. The results were in general agreement with the data in the literature but also showed some differences. They were partially explained because of the higher accuracy of the new optimization strategy but it was also shown that the number of independent experimental stress–strain curves used as input is critical to reach an accurate solution to the inverse optimization problem. It was concluded that at least three independent stress–strain curves are necessary to determine the single crystal behavior from polycrystal tests in the case of highly textured Mg alloys.

1. Introduction

Multiscale modeling of polycrystalline materials has been carried out by homogenization of the single crystal behavior by means of different mean-field methods (Taylor approximation Taylor, 1938, visco-plastic self-consistent model Lebensohn and Tomé, 1993, etc.) or, more recently, using computational homogenization (Miehe et al., 1999, 2002; Segurado et al., 2012; Segurado and LLorca, 2013). The key ingredients to predict accurately the polycrystal behavior are the microstructural details (grain size, shape and orientation distribution) and the mechanical properties of the single crystals. The development of advanced 3D microstructural characterization techniques (such as serial sectioning and X-ray microtomography together

with electron back-scattered diffraction and X-ray diffraction) (Ludwig et al., 2009; Robertson et al., 2011; Fernández et al., 2013; Sket et al., 2014) allows to obtain a very precise microstructural description. However, the main uncertainty during homogenization of the polycrystal behavior comes from the actual properties of the single crystals within the polycrystal, that are difficult to measure.

The physical deformation mechanisms in metallic single crystals have been studied in detail and they are well understood. The elastic behavior is determined by the crystal symmetry and the corresponding elastic constants, which are well known. Plastic deformation is controlled by dislocation slip and, in some cases, by twinning and it can be highly dependent on the crystal orientation, leading to a strong anisotropy in the plastic response. The single crystal behavior is modeled within the continuum viewpoint with crystal plasticity models (Hill, 1966; Rice, 1971; Hill and Rice, 1972), which take into account the geometry of slip and/or twinning for each material and lattice configuration. The response of each slip/twinning system is governed by the critical resolved shear stresses (CRSS) and its evolution with deformation, which is introduced by means of either phenomenological (Asaro and Needleman, 1985; Bassani et al., 1991) or physically-based models (Arsenlis and Parks, 2002; Cheong and Busso, 2004; Ma et al., 2006). Nevertheless, quantitative values of the parameters in these models are difficult to obtain experimentally, limiting the predictive capabilities of the multiscale models.

There are three different approaches available to obtain the quantitative values of the parameters which control the single crystal behavior. The first one is to carry out simple mechanical tests (compression, bending) of microscopic single crystals built from the polycrystal (see Gianola and Eberl, 2009 for a review). This strategy is the most obvious but is very time consuming and it is not clear that the results can be directly used in the simulation of polycrystals because of the presence of size effects. A simpler strategy is based on the use of instrumented nanoindentation of single crystals with different orientation within the polycrystal (Liu et al., 2005; Eidel, 2011). Testing is very straightforward in this case but the interpretation of the experimental data to obtain the parameters which control the behavior of each slip/twinning system is difficult by the complex stress state below the indentor. In addition, nanoindentation results are also size dependent. Another methodology to obtain the single crystal properties is based on a multsicale modeling approach, in which the effect of alloying elements, precipitates or defects and dislocation–dislocation interactions on the CRSS and the subsequent hardening are accounted for using density-functional theory, molecular dynamics or dislocation dynamics. Successful examples of this methodology have appeared recently (Leyson et al., 2010; Barton et al., 2013) but they are still limited in terms of the mechanisms that can be accounted for and of the uncertainties associated with the bridge of time and length scales between the different simulation approaches.

Thus, taking into account the limitations of experiments and theory, the most widely used strategy to obtain the single crystal properties is based on the calibration of the parameters which control the single crystal properties by fitting experimental results of polycrystals loaded in different orientations by means of simulations based on mean-field methods or computational homogenization (Miehe et al., 1999, 2002; Segurado et al., 2012; Segurado and LLorca, 2013; Tomé et al., 2001; Tomé et al., 2002; Fernández et al., 2011; Pei et al., 2011; Knezavic et al., 2010; Wang et al., 2010; Agnew et al., 2001). The main problem with this strategy is that the number of parameters to be determined for each single crystal is very large and finding the optimum parameter set is neither easy nor a unique result is guaranteed. In fact, it is not unusual to find that different authors report different (or even contradictory) values for similar materials. HCP metals are the most typical example of these shortcomings because of the large plastic anisotropy and the coexistence of slip and twinning during plastic deformation. For instance, Table 1 shows the magnitude of the initial CRSS reported by different groups for the most important slip systems (basal, prismatic and pyramidal $c+a$) and extension twinning in AZ31 Mg alloy. The differences are non negligible from the quantitative viewpoint and, in addition, some authors Agnew et al. (2001) and Pei et al. (2011) considered that the initial CRSS for tensile twinning was below the one for basal slip whereas basal was the softest system in other studies (Fernández et al., 2011; Knezavic et al., 2010; Wang et al., 2010), following the behavior of pure Mg. Obviously, these differences have very large implications in the dominant deformation mechanisms (and in the texture development) during deformation and their origin is not easy to assess. Although disparities in grain size or processing parameters could explain some of the differences in the initial CRSS reported on the different studies, the spread in the corresponding experimental results is much smaller than the differences among the CRSS values. This fact suggests that the disparities in the values proposed for the CRSS should also be closely related to the methodology used for the model calibration.

Table 1
Values of the initial CRSS for different slips systems and tensile twinning in AZ31 Mg alloy predicted by fitting experimental results on polycrystals with simulations based on mean-field methods or computational homogenization.

Deformation mode	Reference				
	Fernández et al. (2011)	Pei et al. (2011)	Knezavic et al. (2010)	Wang et al. (2010)	Agnew et al. (2001)
Basal	α	α	α	α	α
Prismatic	9α	2α	5α	5α	–
Pyramidal $c+a$	13α	15α	6α	8α	3α
Twinning	2α	0.7α	2α	2α	0.5α
α (MPa)	9	–	–	15	30
grain size (μm)	13	42	8	–	25–100

Within this framework, this paper is aimed at establishing an objective and efficient methodology to determine the single crystal properties from the macroscopic mechanical behavior of polycrystals in the case of strongly anisotropic HCP metals deforming by slip and twinning. The polycrystal behavior is obtained by means of the finite element simulation of a representative volume element (RVE) of the microstructure and the inverse problem is solved by means of the Levenberg–Marquardt method (Levenberg, 1944; Marquardt, 1963), which is recommended for general non-linear least squares problems in optimization literature (Dennis and Schnabel, 1966). The Levenberg–Marquardt method has been previously used in solid mechanics to solve the Gurson–Tvergaard–Needleman equation of damage for ductile fracture of metals (Shterenlikht and Alexander, 2012) as well as inverse problems dealing with the thermal conductivity and heat capacity in orthotropic materials (Sawaf et al., 1995) or the plastic deformation parameters in metal forming (de-Carvalho et al., 2011). More recently, it was successfully applied to identify the single crystal parameters of FCC polycrystalline metals (Evrard et al., 2010; Bui et al., 2013). It should be noted, however, that the optimization problem in FCC materials is rather simple (as compared to HCP crystals) because there is only one active slip system and the single crystal behavior is fairly isotropic. Moreover, the polycrystal behavior in these studies was determined using analytical or semi-analytical homogenization models (iso-strain or viscoplastic self-consistent), while computational homogenization (which provides higher accuracy in the simulation) is used in this investigation.

The paper is organized as follows. After the introduction, the crystal plasticity model and computational homogenization strategy for the polycrystal are presented in Section 2. Section 3 is devoted to detail the inverse optimization methodology and the application to AZ31 Mg alloy will be shown and discussed in Section 4. The main conclusions of the paper can be found in Section 5.

2. Finite element crystal plasticity model

2.1. Crystal plasticity model

The crystal plasticity model developed in Segurado and LLorca (2013) and implemented as a UMAT in the finite element code ABAQUS (Abaqus, 2013) is the basis of this work. It has been adapted to account for the plastic deformation features of Mg alloys including basal, prismatic and pyramidal slip and extension twinning. The model assumes a multiplicative decomposition of the deformation gradient into the elastic and plastic parts (Lee and Liu, 1967) according to,

$$\mathbf{F} = \mathbf{F}^e\mathbf{F}^p \tag{1}$$

where the configuration defined by $\mathbf{F}^p$ is called the relaxed or intermediate configuration (Fig. 1).

From the definition of the velocity gradient, $\mathbf{L}$, expression (1) leads to

$$\mathbf{L} = \dot{\mathbf{F}}\mathbf{F}^{-1} = \dot{\mathbf{F}}^e\mathbf{F}^{e^{-1}} + \mathbf{F}^e\dot{\mathbf{F}}^p\mathbf{F}^{p^{-1}}\mathbf{F}^{e^{-1}} \tag{2}$$

where $\mathbf{L}^p = \dot{\mathbf{F}}^p\mathbf{F}^{p^{-1}}$ stands for the plastic deformation rate in the intermediate configuration.

The plastic deformation is accommodated by slip and twinning and N_{sl} and N_{tw} stand for the total number of slip and twin systems available, respectively. Twinnning is included in the crystal plasticity framework using the model developed by Kalidindi (1998). A material point is divided into two phases, a parent region and a twinned region (Fig. 1), which is formed by a maximum of N_{tw} subregions. Each subregion belongs to a given twinning system α and its volume fraction is f^α. Thus, the parent region volume fraction is given by $1 - \sum_{\alpha=1}^{N_{tw}} f^\alpha$.

The material point is considered a *composite* material in which the iso-strain hypothesis holds ($\mathbf{F}$ and $\mathbf{F}^\alpha$ are the same in all phases). The plastic deformation is the result of three mechanisms and the plastic velocity gradient in the intermediate configuration contains three terms. The slip in the parent phase, $\mathbf{L}^p_{sl}$, is given by

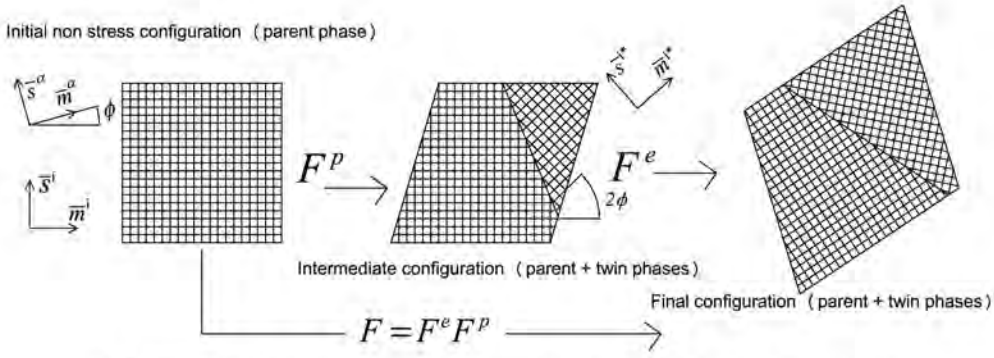

Fig. 1. Multiplicative decomposition indicating material point subdivision in parent and twin phases.

$$\mathbf{L}_{sl}^{p}=\left(1-\sum_{\alpha=1}^{N_{tw}}f^{\alpha}\right)\sum_{i=1}^{N_{sl}}\dot{\gamma}^{i}\mathbf{m}_{sl}^{i}\otimes\mathbf{s}_{sl}^{i} \tag{3}$$

where $\mathbf{s}_{sl}^{i}$ and $\mathbf{m}_{sl}^{i}$ stand, respectively, for the unit vectors in the slip and normal direction to the slip plane considered in the intermediate configuration.

The second contribution, $\mathbf{L}_{tw}^{p}$, is the rate of deformation due to the twin transformation of a differential volume fraction of parent phase $\mathrm{d}f^{\alpha}$

$$\mathbf{L}_{tw}^{p}=\sum_{\alpha=1}^{N_{tw}}\dot{f}^{\alpha}\gamma_{tw}\mathbf{m}_{tw}^{\alpha}\otimes\mathbf{s}_{tw}^{\alpha} \tag{4}$$

where $\dot{f}^{\alpha}=\mathrm{d}f^{\alpha}/\mathrm{d}t$ is the rate of the volume fraction transformation in the twin system α, $\mathbf{m}_{tw}^{\alpha}$ and $\mathbf{s}_{tw}^{\alpha}$ are the unit vectors defining the twinning system and γ_{tw} is the characteristic shear of the twinning mode (in the case of tension twinning of Mg alloys, $\gamma_{tw}=0.129$). It should be noted that extension twinning is a polar mechanism and it will only take place when the applied deformation leads to extension of the c axis of the HCP lattice.

Finally, the third contribution corresponds to the slip of the transformed regions (denominated *re-slip*), $\mathbf{L}_{re-sl}^{p}$, which can be expressed as,

$$\mathbf{L}_{re-sl}^{p}=\sum_{\alpha=1}^{N_{tw}}f^{\alpha}\left(\sum_{i'=1}^{N_{sl-tw}}\dot{\gamma}^{i'}\mathbf{m}_{sl}^{i'}\otimes\mathbf{s}_{sl}^{i'}\right) \tag{5}$$

where $\mathbf{m}_{sl}^{i'}$ and $\mathbf{s}_{sl}^{i'}$ stand for the unit vectors in the slip and normal directions to the slip plane considered i re-oriented due to the rotation $\mathbf{Q}^{\alpha}$ produced by twinning across the twin system α,

$$\mathbf{Q}^{\alpha}=2\mathbf{m}_{tw}^{\alpha}\otimes\mathbf{m}_{tw}^{\alpha}-\mathbf{I} \tag{6}$$

where $\mathbf{I}$ is the second order identity tensor. It has been experimentally observed (Fernández et al., 2011) that the volume fraction of twinned regions in AZ31 Mg alloy reaches a maximum around $\sum f^{\alpha}\approx 0.80$. Thus, the *re-slip* term was activated at a given material point when the volume fraction of the twinned material at this point reached 0.80. Also notice that the number of systems considered for *re-slip*, N_{sl-tw}, may be different from the number of original slip systems N_{sl} for simplicity.

The crystal was assumed to behave as an elasto-viscoplastic solid in which the plastic slip rate for a given slip system follows a power-law, according to Hutchinson (1976),

$$\dot{\gamma}^{i}=\dot{\gamma}_{0}\left(\frac{|\tau^{i}|}{g^{i}}\right)^{\frac{1}{m}}\mathrm{sign}(\tau^{i}) \tag{7}$$

where $\dot{\gamma}_{0}$ is a reference shear strain rate, g^{i} the CRSS of the slip system i, m the rate-sensitivity exponent and τ^{i} the resolved shear stress on the slip system i.

Similarly, the twinning rate, $\dot{f}$, also follows a viscous law

$$\dot{f}^{\alpha}=\dot{f}_{0}\left(\frac{\langle\tau^{\alpha}\rangle}{g^{\alpha}}\right)^{\frac{1}{m}}\quad\text{with}\quad\langle\tau\rangle=\begin{cases}\tau & \text{if } \tau\geqslant 0\\ 0 & \text{if } \tau<0\end{cases} \tag{8}$$

and the transformation rate is set equal to zero if the volume fraction of twinned material exceeds a saturation value of 0.80 (Kalidindi, 1998). Mathematically,

$$\dot{f}^{\alpha}=0\ \text{if}\ \sum_{\alpha=1}^{N_{tw}}f^{\alpha}\geqslant 0.80 \tag{9}$$

Because of the iso-strain approach, the parent and twinned phases at a given material point are deformed under the same $\mathbf{F}$ and $\mathbf{F}^{e}$ and they share the same elastic strain in the intermediate configuration, given by the Green–Lagrange strain tensor, $\mathbf{E}^{e}$,

$$\mathbf{E}^{e}=\frac{1}{2}\left(\mathbf{F}^{e^{T}}\mathbf{F}^{e}-\mathbf{I}\right). \tag{10}$$

The symmetric second Piola–Kirchhoff stress tensor in the intermediate configuration, $\mathbf{S}$, is obtained in this case from the volume-averaged stress tensors in the different phases

$$\mathbf{S}=\left(1-\sum_{\alpha=1}^{N_{tw}}f^{\alpha}\right)\mathbf{S}^{parent}+\sum_{\alpha=1}^{N_{tw}}f^{\alpha}\mathbf{S}^{\alpha} \tag{11}$$

and the stresses on the parent ($\mathbf{S}^{parent}$) and twinned ($\mathbf{S}^{\alpha}$) phases are given by

$$\begin{aligned}\mathbf{S}^{parent}&=\mathbb{C}\mathbf{E}^{e}\\ \mathbf{S}^{\alpha}&=\mathbb{C}^{\alpha}\mathbf{E}^{e}\end{aligned} \tag{12}$$

where $\mathbb{C}$ stands for the fourth order elastic stiffness tensor of the crystal in its original orientation and $\mathbb{C}^{\alpha}$ are the corresponding stiffness tensors reoriented after twinning. They are given by,

$$\mathbb{C}^{\alpha}_{ijkl} = \mathbb{C}^{\alpha}_{pqrs} Q^{\alpha}_{ip} Q^{\alpha}_{jq} Q^{\alpha}_{kr} Q^{\alpha}_{ls} \tag{13}$$

The resolved shear stress on a slip (τ^i) or twinning (τ^{α}) in the parent (i) region is obtained as,

$$\tau^i = \mathbf{S}^{parent} : \mathbf{m}^i_{sl} \otimes \mathbf{s}^i_{sl} \quad \text{with} \quad \tau^{\alpha} = \mathbf{S}^{parent} : \mathbf{m}^{\alpha}_{tw} \otimes \mathbf{s}^{\alpha}_{tw} \tag{14}$$

while the resolved shear stress on a slip plane in the twinned region ($\tau^{i'}$) is given by,

$$\tau^{i'} = \mathbf{S}^{\alpha} : \mathbf{m}^{i'}_{sl} \otimes \mathbf{s}^{i'}_{sl} \tag{15}$$

Finally, the Cauchy stress can be approximated as

$$\boldsymbol{\sigma} = J^{-1} \mathbf{F}^e \mathbf{S} \mathbf{F}^{eT} \approx \mathbf{R}^e \mathbf{S} \mathbf{R}^{eT} \tag{16}$$

under the assumption of small elastic deformations, where $J = \det(\mathbf{F})$ and $\mathbf{R}^e$ stands for the orthogonal rotation tensor obtained by the polar decomposition of $\mathbf{F}^e$.

Finally, the constitutive equation for each slip and twinning system has to be defined. It is given by the initial value of CRSS to activate slip (τ^i_0) or twinning (τ^{α}_0) in each system and the corresponding hardening laws. A phenomenological hardening model, which is able to reproduce the different stages of single crystal deformation, was adopted to this purpose (Kothary and Anand, 1998). The evolution of the CRSS g^i, g^{α}, $g^{i'}$ for both slip, twin and re-slip systems are given by Eqs. (17)–(19), respectively, which are shown below,

$$\dot{g}^i = q_{sl-sl} \sum_{j=1}^{N_{sl}} h_{0j} \left(1 - \frac{\tau^j}{\tau^j_{sat}}\right)^{a_{sl}} |\dot{\gamma}^j| + q_{tw-sl} \sum_{\beta=1}^{N_{tw}} h_{0tw} \left(1 - \frac{\tau^{\beta}}{\tau^{tw}_{sat}}\right)^{a_{tw}} |\dot{\gamma}^{\beta}| \tag{17}$$

$$\dot{g}^{\alpha} = q_{tw-tw} \sum_{\beta=1}^{N_{tw}} h_{0tw} \left(1 - \frac{\tau^{\beta}}{\tau^{tw}_{sat}}\right)^{a_{tw}} \dot{f}^{\alpha\gamma} \dot{\gamma}^{\gamma}_{tw} \tag{18}$$

$$\dot{g}^{i'} = q_{sl-sl} \sum_{j=1}^{N_{re-sl}} h_{0j} \left(1 - \frac{\tau^j}{\tau^j_{sat}}\right)^{a_{sl}} |\dot{\gamma}^j| \tag{19}$$

where different parameters in these equations define the contributions arising from self-hardening and latent hardening. The self-hardening of a given slip (sl) or twinning (tw) system is dictated by three terms: the saturation stress, τ_{sat}, the initial hardening rate h_0 and the hardening exponent a. The latent-hardening contribution to slip due to slip in other systems is introduced with the coefficient q_{sl-sl} whereas the contribution induced by twinning is given by q_{tw-sl}. The model only takes into account the effect of twinning on slip and it is assumed that slip does not influence twinning ($q_{sl-tw} = 0$) (Capolungo et al., 2009; Zhang and Joshi, 2012).

Three slip systems (basal, prismatic and pyramidal $c + a$) and extension twinning were included in the model to simulate the deformation of AZ31 Mg alloy. They are depicted in Fig. 2.

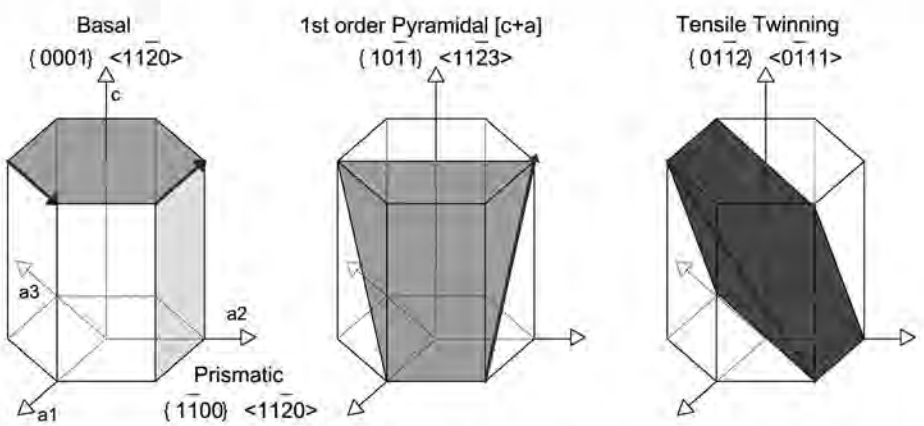

Fig. 2. Deformation modes included in the single crystal model: basal, prismatic and pyramidal $c + a$ slip as well as extension twinning.

2.2. Computational homogenization framework

2.2.1. Microstructure representation

The effective properties of a polycrystalline AZ31 Mg alloy manufactured by hot rolling were determined through the finite element simulation of an RVE of the microstructure. Several representations of the microstructure were used, which were based on a cubic RVE discretized with cubic finite elements (voxels). In three models, each crystal in the RVE was represented by one voxel and the models differed in the number of crystal included in the RVE, either 64, Fig. 3(a), 216 or 512, Fig. 3(b). Simplicity in the RVE generation and the possibility to include a large number of grains in the RVE with limited computational cost are the obvious advantages of this representation. However, it is known that the models with one voxel per crystal tends to give a stiff response (Segurado and LLorca, 2013; Zhao et al., 2007) because the deformation is overconstrained to maintain the compatibility between adjacent crystals. This fact is enhanced by the poor representation of the strain fields because the linear finite elements cannot reproduce the strain concentrations at the grain boundaries (Segurado and LLorca, 2013; Zhao et al., 2007). Nevertheless, this RVE provides a fast route to obtain an initial prediction of the aggregate behavior.

The limitations of the representation described above can be overcome with a more realistic description of the microstructure in which each single crystal is discretized with several cubic elements, Fig. 3(c). The subdivision of the grain with several finite elements reduces the constrain imposed by neighboring grains and leads to a better representation of the strain gradients. In addition, features associated with grain shape and size distributions can be included. This RVE contained 584 grains and was created with the microstructure generator Dream3D (Dream3D, 2012). On average, each grain was discretized with 7 voxels. The grains were equiaxed and the grain size followed a log-normal distribution with an average grain volume equal to the RVE divided by 584. Obviously, this representation is more accurate than the previous ones but the computational cost is much higher. The grain orientation in all RVEs was determined from the experimental orientation distribution function (ODF) of the initial texture. The orientation of each grain was obtained by a Monte Carlo lottery and the larger the number of grains, the higher the accuracy in the model texture.

Four types of RVE were hierarchically used in the optimization process, 64×1, 216×1, 512×1 and 584×7. The first number indicates the number of the crystals in the RVE and the second the number of voxels to represent each crystal. The initial predictions of the single crystal properties were carried out using the models with one voxel per crystal (starting with 64×1, followed by 216×1 and 512×1). These models were computationally efficient and provided a good estimation of the single crystal properties, which was used as a starting point of most accurate (and computationally expensive) optimization carried out with the 584×7 representation. This was particularly useful in the case of rolled AZ31 Mg alloy, because the results obtained with different RVEs were rather similar as a result of the strong texture, which dominates the macroscopic behavior. Nevertheless, it has been shown that the macroscopic response of the one voxel per grain RVEs can be inaccurate in the case of HCP polcrystals with random texture (Segurado and LLorca, 2013) and thus the hierarchical optimization process may not be as efficient in other cases.

2.2.2. Finite element simulation of the RVE

The mechanical behavior of the polycrystalline RVE was obtained by the finite element method. Periodic boundary conditions were applied on the cubic cell faces because the homogenized polycrystal behavior derived under these conditions is always closer to the exact solution (provided by an RVE of infinite dimensions) than those obtained with imposed displacements or forces (Segurado and LLorca, 2002). The periodic boundary conditions assume that the RVE deforms as a jigsaw puzzle and that the whole space can be filled with a periodic translation of the RVE along the three Cartesian axes. If the initial cube length is L, and the origin of coordinates is located at one corner, the three concurrent edges of the cubic RVE define an orthogonal basis $\mathbf{e}_1$, $\mathbf{e}_2$ and $\mathbf{e}_3$ with corresponding coordinates x_1, x_2, x_3. The periodic boundary conditions link

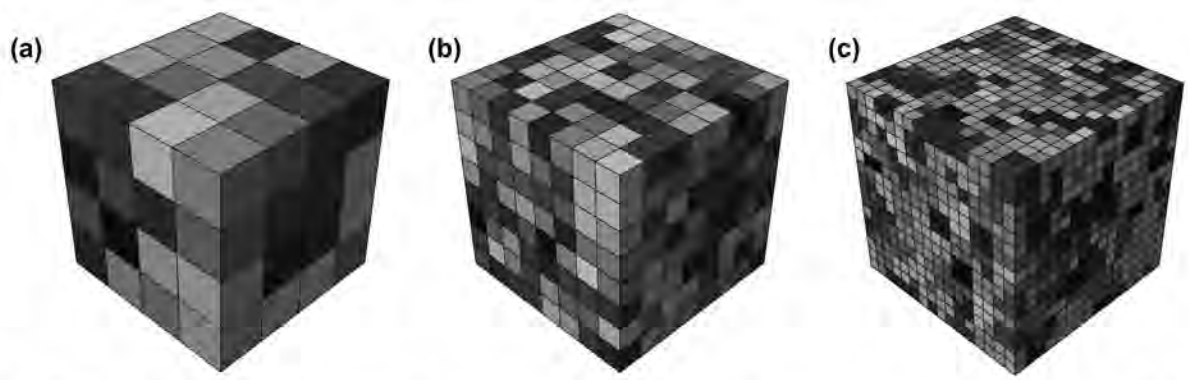

Fig. 3. Different RVE of the polycrystal microstructure. (a) Voxel representation with 64 cubic finite elements in which each one stands for a grain. (b) Voxel representation with 512 cubic finite elements, one per grain. (c) Realistic RVE containing 584 crystals discretized with ≈7 cubic finite elements per grain.

the local displacement vector $\mathbf{u}$ of the nodes on opposite faces of the cubic RVE with the far-field macroscopic deformation gradient $\bar{\mathbf{F}}$ according to,

$$\begin{aligned}
\mathbf{u}(x_1, x_2, 0) - \mathbf{u}(x_1, x_2, L) &= (\bar{\mathbf{F}} - \mathbf{I})\mathbf{l}_3 \\
\mathbf{u}(x_1, 0, x_3) - \mathbf{u}(x_1, L, x_3) &= (\bar{\mathbf{F}} - \mathbf{I})\mathbf{l}_2 \\
\mathbf{u}(0, x_2, x_3) - \mathbf{u}(L, x_2, x_3) &= (\bar{\mathbf{F}} - \mathbf{I})\mathbf{l}_1
\end{aligned} \tag{20}$$

where $\mathbf{l}_i = L\mathbf{e}_i$. The far-field deformation gradient $\bar{\mathbf{F}}$ applied to the RVE is obtained by prescribing the displacements of three master nodes M_i corresponding to three different faces of the RVE,

$$\mathbf{u}(M_i) = (\bar{\mathbf{F}} - \mathbf{I})\mathbf{l}_i. \tag{21}$$

If some components of the far-field deformation gradient are not known *a priori* (mixed boundary conditions, as in under uniaxial tension), the corresponding components of the effective stresses $\bar{\boldsymbol{\sigma}}$ are set instead. This is carried out by applying a nodal force P_j to the master node M_i and degree of freedom j according to

$$P_j(M_i) = (\bar{\boldsymbol{\sigma}}\mathbf{e}_i)_j A_i \tag{22}$$

where A_i is the projection of the current area of the face perpendicular to $\mathbf{e}_i$ in this direction.

Finally, the macroscopic Cauchy stresses acting on any cube surface can be computed by dividing the reaction forces F_j of the master nodes M_i by the actual area of the face perpendicular to that master node A_i.

$$\bar{\sigma}_{ij} = \frac{F_j}{A_i} \tag{23}$$

3. Optimization strategy

The mechanical behavior of the polycrystal can be obtained by the finite element simulation of the RVE and compared with the experimental results. The objective of the optimization strategy is to obtain the value of the parameters which determine the behavior of the single crystal (the initial CRSS in each slip or twinning system and those included in the hardening laws given by Eqs. (17)–(19)) which provide the best possible fit between the numerical simulations of the polycrystal and the experimental data. The optimization process is a challenge because of the large number of parameters and of the strong non-linearity of the problem, which is more critical in the case of anisotropic crystals which deform by slip and twinning.

The optimization procedure is based on the Levenberg–Marquardt method (Levenberg, 1944; Marquardt, 1963), which was adapted to be used in the context of polycrystal homogenization. Let $x_i,\ y_i$ be a set of n points defining some experimental result (i.e. strain–stress curve of the polycrystal) and let $y = f(x; \boldsymbol{\beta})$ be the model prediction of that experiment which is defined by a set of m parameters $\boldsymbol{\beta}$. The Levenberg–Marquardt method is an optimization method to obtain the set of parameters $\boldsymbol{\beta}$ that minimizes the objective function $O(\boldsymbol{\beta})$ defined as

$$O(\boldsymbol{\beta}) = \sum_{i=1}^{n} |y_i - f(x_i,\ \boldsymbol{\beta})| = \|\mathbf{y} - \mathbf{f}(\boldsymbol{\beta})\|. \tag{24}$$

Assuming a small perturbation of the model parameters $\boldsymbol{\delta}$, the model can be linearized with respect to the perturbation and the new model response can be written as,

$$\mathbf{f}(\boldsymbol{\beta} + \boldsymbol{\delta}) \approx \mathbf{f}(\boldsymbol{\beta}) + \mathbf{J}\boldsymbol{\delta} \tag{25}$$

where

$$J_{ij} = \frac{\partial f(x_i, \boldsymbol{\beta})}{\partial \beta_j} \quad \text{with} \quad 1 \leqslant i \leqslant n \quad \text{and} \quad 1 \leqslant j \leqslant m \tag{26}$$

is the Jacobian matrix, obtained by evaluating the derivatives of f with respect to the set of parameters $\boldsymbol{\beta}$ on the points x_i. Thus, the value of the objective function O at the point $\boldsymbol{\beta} + \boldsymbol{\delta}$ can be written as

$$O(\boldsymbol{\beta} + \boldsymbol{\delta}) \approx \|\mathbf{y} - \mathbf{f}(\boldsymbol{\beta}) - \mathbf{J}\boldsymbol{\delta}\|. \tag{27}$$

Levenberg and Marquardt minimized this objective function by adding a dumping factor λ to the usual expression of steepest descent (Levenberg, 1944; Marquardt, 1963), leading to the following linear set of equations

$$(\mathbf{J}^T\mathbf{J} + \lambda \operatorname{diag}(\mathbf{J}^T\mathbf{J}))\boldsymbol{\delta} = \mathbf{J}^T[\mathbf{y} - \mathbf{f}(\boldsymbol{\beta})] \tag{28}$$

whose solution $\boldsymbol{\delta}$ provides the new set of parameters that minimizes the objective function. In the absence of the dumping parameter λ, the iterative process to solve the non-linear set of equations often stops because the Jacobian matrix becomes singular. This drawback can be overcome with the addition of the (non-negative) damping factor, λ, which is adjusted at each iteration. If the reduction of the objective function O is rapid, smaller values of λ can be used in each iteration, bringing the

algorithm closer to the fast Gauss–Newton algorithm. On the contrary, higher λ values can be used when the objective function O is not reduced. This procedure is repeated iteratively until the error in the objective function reaches the desired value. In each iteration, the Jacobian matrix $\mathbf{J}$ (Eq. (26)) has to be computed, the damping parameter selected and the linear set of equations in (28) solved.

3.1. Adaptation to computational homogenization of polycrystals

The Levenberg–Marquardt method can be easily applied if there is an analytical expression of f and its derivatives. In the case of computational homogenization, the function $y_i = f(x_i; \boldsymbol{\beta})$ is the macroscopic stress–strain curve of the polycrystal under certain boundary conditions which is obtained by the finite element analysis of the RVE with a set of parameters $\boldsymbol{\beta}$ which define the single crystal properties. In fact, the function f often includes simulations in different orientations (different boundary conditions) to be compared with the corresponding experimental data sets to improve the accuracy of the parameter identification. The most obvious sets of experimental data are stress–strain curves obtained under different conditions (orientation, tension/compression, etc.) and this was the strategy adopted in this investigation. However, the optimization procedure can also be extender to other metrics, such as the final texture at the end of deformation. In this case, each region of the orientation space will correspond to x_i and the corresponding volume fraction of crystals oriented in that direction will be given by y_i.

In order to compute the Jacobian matrix (Eq. (26)), one of the parameters is perturbed by $\Delta\beta_j$

$$\boldsymbol{\beta}^{*j} = \boldsymbol{\beta} + \{0, 0, \ldots, \Delta\beta_j, \ldots, 0\}^T \tag{29}$$

and the response of the perturbed model, $f(x_i; \boldsymbol{\beta}^{*j})$, is determined by the finite element analysis of the RVE. This procedure is repeated for each parameter in the model and the resulting Jacobian matrix is given by,

$$J_{ij} = \frac{\partial f(x_i; \boldsymbol{\beta})}{\partial \beta_j} \approx \frac{f(x_i; \boldsymbol{\beta}^{*j}) - f(x_i; \boldsymbol{\beta})}{\Delta\beta_j} \tag{30}$$

The ability of the Levenberg–Marquardt method to find global minimizers of the error will depend on the parameter λ chosen on each iteration. Starting with an arbitrary value (e.g. $\lambda = 1$) in the first iteration, three different damping parameters, corresponding to 2λ, λ and 0.5λ, are selected and the objective function (Eq. (24)) is computed for the three damping parameters. The damping parameter which leads to a minimum error O is selected as the starting damping parameter for the next iteration and the procedure is repeated until the objective function O is below a given tolerance or when the difference in the error between two consecutive steps is negligible. In the latter case, the new λ to begin the next iteration will be either 8 times higher or smaller than the previous one. It will be higher if the smallest error was achieved when optimization was carried out using 2λ as the damping constant and it will be smaller if the smallest error was obtained with 0.5λ.

The optimization algorithm based on the Levenberg–Marquardt method has been programmed in Python and runs as an Abaqus (Abaqus, 2013) script that reads all the necessary input information (experimental stress–strain curves, microstructural information, etc.) and automatically executes the different tasks in the optimization process: generation of the input files for the finite element analysis with the perturbed parameters, execution and post-processing of the finite element simulations of the RVE, assembly of the Jacobian matrix, selection of damping parameters, solving of the linear equation set for the new set of parameters, and checking whether the error in the objective function has reached the desired limit to finish the process or begin another iteration. It should be noted that different RVEs were used in the optimization loop to speed up the process. The first iterations were performed with RVEs containing 1 voxel per crystal, Fig. 3(a) and (b). The best parameters obtained with these RVEs were used as input for the more realistic RVE of the microstructure, Fig. 3(c).

4. Results and discussion

4.1. Material and experimental results

The methodology presented above was applied to determine the single crystal properties of a polycrystalline AZ31 Mg alloy at room temperature. The material was obtained from a 1 in-thick plate processed by hot rolling (Dogan et al., 2013). The average grain size was 25 μm and the pole figure of the as-rolled material is plotted in Fig. 4(a). It shows the strong basal texture typical of rolled Mg alloys, with the c axis parallel to the normal direction (ND). Also, the spread prismatic poles appear along the rolling (RD) and transverse (TD) directions.

Specimens for tension and compression experiments along different orientations were machined from the plate. Flat dogbone specimens were used for the tensile tests and the dimensions of the gage section were $8 \times 3 \times 1.5$ mm^3. Compression specimens were rectangular prisms with the dimensions of $4 \times 4 \times 8$ mm^3. Mechanical tests were carried out using an MTS test frame at an average strain rate of 5×10^{-4} s^{-1}. Strains were measured with extensometers of 8 mm and 3 mm gauge length, which were attached to the tension and compression specimens, respectively. The material was deformed in uniaxial compression and uniaxial tension along ND and also in uniaxial tension along RD. An additional test was carried out in uniaxial tension in the RD-ND plane at 45° from both orientations (Fig. 5). Three tests were carried out in each orientation and/or loading direction (tension/compression.

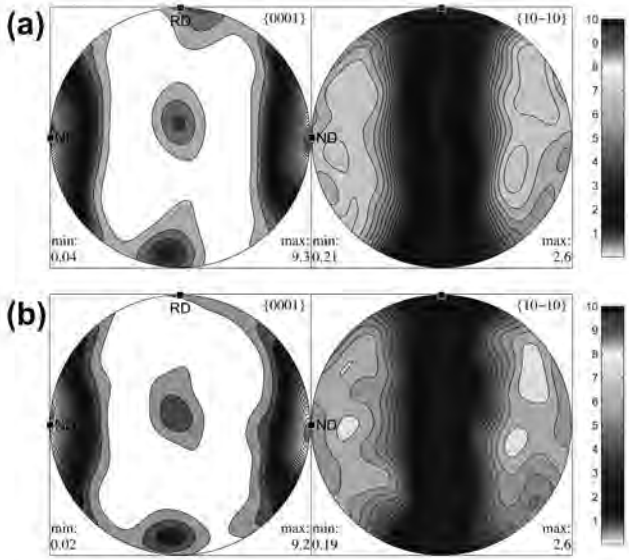

Fig. 4. Pole figures of rolled AZ31 Mg alloy. (a) Experimental initial texture. (b) Reduced equivalent initial texture with 584 orientations used as input to create the RVE. The numbers in the legend stand for multiples of random distribution.

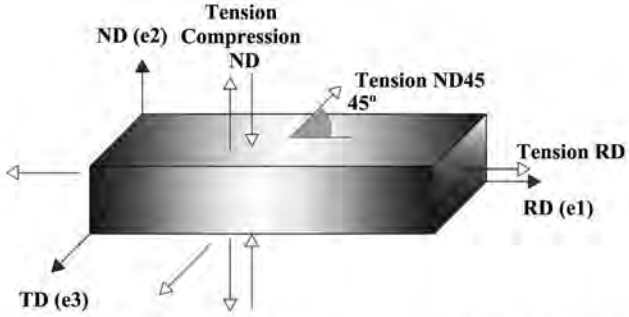

Fig. 5. Schematic of the loading directions for the mechanical tests of the rolled plate of AZ31 Mg alloy.

The true stress–true strain curves in tension and compression in the ND, and in tension in the RD directions are plotted in Fig. 6, together with the ones corresponding to the tensile tests in the RD-ND plane at 45° from both orientations. The three experimental curves for each test are included and they show that the experimental scatter was minimum. These curves show the strong plastic anisotropy of Mg alloys, which is triggered by the limited number of slip systems and by the polar nature of extension twinning, which is only activated when deformation leads to an extension of the *c* axis. As a result, deformation of wrought Mg alloys is markedly dependent on the orientation, and different slip systems (and in different order) are activated as a function of the loading direction (either tension or compression).

4.2. Optimized values of the CRSS

The accuracy of the optimization procedure depends on the input information used to compute the single crystal properties, namely the direction (tension or compression) and orientation of the mechanical tests of the polycrystal. It is obvious that if one of the slip/twinning system is not activated in any of the input mechanical tests, it will be impossible the determine accurately the properties of this system. Thus, the mechanical tests have to be independent (should lead to the activation of different deformation mechanisms) and the minimum number of tests to characterize the single crystal behavior will depend on the number of active slip and twinning systems. Most papers devoted to determine the single crystal properties of Mg alloys use two independent stress–strain curves of polycrystal (Fernández et al., 2011; Wang et al., 2010; Agnew et al., 2001) but it is not demonstrated that this number is enough. The critical test to find out the minimum number of independent curves is to use the single crystal parameters provided by the optimization procedure to predict the mechanical response of the polycrystal in a different orientation/direction.

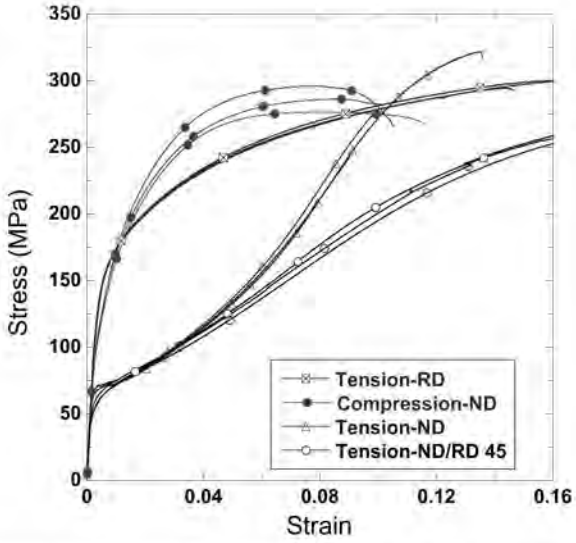

Fig. 6. Experimental true stress–true strain curves of the AZ31 Mg alloy along different orientations.

Table 2
Average values of the maximum Schmid factors for different deformation modes in the polycrystalline AZ31 Mg alloy.

Deformation mode	Schmid factor			
	ND tension	ND compression	RD tension	RD/ND45 tension
Basal	0.25	0.25	0.22	0.34
Prismatic	0.15	0.15	0.39	0.29
Pyramidal	0.46	0.46	0.46	0.43
Twinning	0.36	0.07	0.07	0.25

Whether different mechanical tests on the polycrystal can be considered independent depends on the average value of the Schmid factor for each slip/twinning system with respect to the loading direction. This information can be obtained from the experimental orientation distribution function (Fig. 4(a)) by averaging the Schmid factors for each slip/twinning system over all the grains in the microstructure for each loading case. The average values of the maximum Schmid factor for each deformation mode are found in Table 2.[1]

Tension and compression tests along ND are suitable to promote deformation by basal and pyramidal slip but they are independent because extension twinning is likely to occur in tension but not in compression. In addition, prismatic slip will not be dominant along the ND direction because basal slip and twinning under tension have higher Schmid factors but it is likely to play a major role under RD tension. Thus, these three mechanical tests are good input candidates for the optimization procedure. The table also includes the average values of the maximum Schmid factor for the tests carried out in the RD-ND plane at 45° from both orientations. This case, in which all deformation modes can be active, will be used to validate the optimization procedure.

As indicated above, four different RVEs were used in a hierarchical sequence in the optimization process. The first three RVEs used 1 voxel per grain and included 64, 216 and 512 grains, respectively. The fourth RVE model with a realistic representation of grain shape contained ≈7 voxels per grain and 584 grains. In all cases, each voxel was a cubic finite element (C3D8) in Abaqus with 8 nodes at the cube corners and full integration. The orientation of each grain in the RVEs was obtained from the experimental orientation distribution function (which describes the initial texture) using a Monte Carlo lottery. The maximum number of orientations in the RVEs was limited (584) and the pole figure describing the texture of an RVE with 584 grains, depicted in Fig. 4(b), presented some differences with actual pole figure but captured the strong fiber texture which was the dominant feature. In agreement with previous results (Segurado and LLorca, 2013), it was the mechanical behavior obtained with 584 crystals was independent of the particular random realization obtained from the ODF.

The crystal-plasticity model introduced in Section 2 was used as the constitutive response of the AZ31 Mg grains. The five independent elastic constants of the HCP Mg at 300 K were used here for the AZ31 Mg alloy (Zhang and Joshi, 2012): C_{11} = 59.4 GPa, C_{33} = 61.6, C_{44} = 16.4 GPa, C_{12} = 25.6 GPa, C_{13} = 21.4 GPa. The single crystal parameters to be obtained by

[1] Each deformation mode includes different slip systems. For instance, prismatic slip encompasses $(01\bar{1}0)[2\bar{1}\bar{1}0]$, $(10\bar{1}0)[\bar{1}2\bar{1}0]$ and $(\bar{1}100)[11\bar{2}0]$. So, the average Schmid factor corresponding to each slip system was computed and the maximum of all the averages is listed in Table 2 for each deformation mode and loading case.

the inverse optimization procedure were the initial CRSS, τ_0, the saturation CRSS, τ_s, and initial hardening modulus, h_0, for each deformation mode considered in the model: basal, prismatic and pyramidal $c+a$ slip and extension twinning. The parameters controlling the latent-hardening, q_{sl-sl} and q_{sl-tw}, were 1.0 and 2.0 respectively. These values are in agreement with those used in other investigations (Kothary and Anand, 1998; Staroselsky et al., 1998; Anand, 2004; Roters et al., 2010; Fernández et al., 2011; Wang et al., 2010) and take into account the strong hardening induced by twinning of the traditional slip systems. The hardening exponents a_{sl} and a_{tw} were 0.6 and 1.0 respectively, which are also typical for AZ31 Mg alloy (Fernández et al., 2011). The rate sensitivity exponent, m, in Eq. (7), was 0.1. With this value of m, the mechanical response is independent of the strain rate when the applied strain rates in the simulation are of the order of γ_0. Reducing more the value of m impaired the convergency and led to the same mechanical behavior.

The finite element simulations to compute the polycrystal behavior were carried out in Abaqus/standard (Abaqus, 2013) within the framework of the finite deformations theory with the initial unstressed state as reference. From the available experimental results, three tests were chosen as inputs for the optimization procedure (tension-ND, compression-ND and tension-RD) and the fourth one (tension in the RD-ND plane at 45°) was used to validate the single crystal properties obtained by optimization. The objective function O was built from the experimental stress–strain curves in three directions which, as reported in Table 2, activate different deformation mechanisms. Approximately 200 points per stress–strain curve were used to build the objective function. The optimization procedure began using the RVE with 64 grains and literature data for pure Mg (obtained from Zhang and Joshi (2012) and shown in Table 3) were used for the 12 unknown parameters.

The evolution of the error in the optimization procedure (given by objective function, Eq. (24), divided by number of points n in the data set) with the number of iterations is plotted in Fig. 7. It shows that the error decreased rapidly with

Table 3
Optimum values of the parameters that define the mechanical behavior of each slip system and extension twinning in the AZ31 Mg alloy as a function of the RVE used in the optimization process. Magnitudes are expressed in MPa.

Parameter	Deformation mode	Initial values	RVE		
			64 Grains 64 voxels	512 Grains 512 voxels	584 Grains 4096 voxels
τ_0	Basal	1.75	11	20	23
	Prismatic	25	87	80	80
	Pyramidal c + a	40	93	83	88
	Twinning	3.5	22	34	35
τ_s	Basal	40	13	23	25
	Prismatic	85	101	94	94
	Pyramidal c + a	150	168	171	179
	Twinning	20	24	64	59
h_0	Basal	20	1	20	20
	Prismatic	1500	2831	2831	2831
	Pyramidal c + a	3000	3817	2990	2990
	Twinning	100	13	24	24

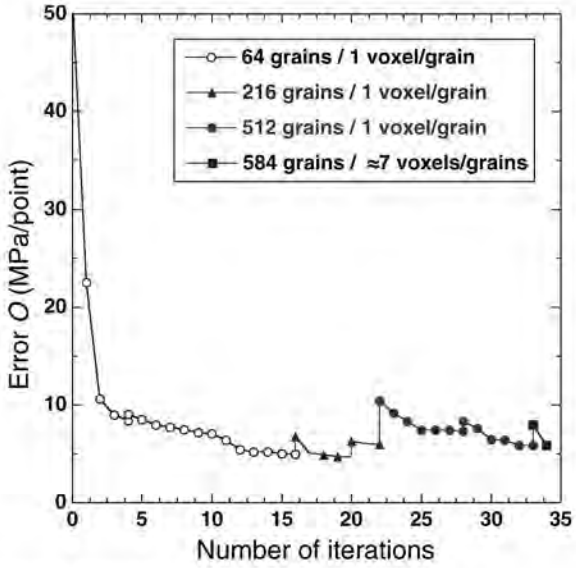

Fig. 7. Evolution of the objective error function per point as a function of the number of optimization iterations for different RVEs.

the number of iterations but reached a plateau after 10 iterations. At this point, the dumping parameter λ (Eq. (28)) begins to grow and further iterations do not reduce the error, indicating that the optimum has been reached for the RVE considered. Then, another set of iterations was carried out using the parameters obtained in the last simulation with the RVE containing 216 grains and afterwards with the RVE with 512 crystals. The initial error at the beginning of each set of iteration with a new RVE was higher because the parameters were optimized for the previous RVE but the differences were not large indicating that the models with one voxel per grain provided a good approximation in this strongly textured material. The final set of iterations was carried out with the realistic RVE containing 584 grains and ≈7 voxels per grain and the results obtained after two iterations with this model were considered optimum.

The optimum values of the parameters to describe the mechanical behavior of each slip system and extension twinning are shown in Table 3 for the RVEs with 64, 512 and 584 grains. They were very different from the initial ones, corresponding to pure Mg, but the disparities in the parameters obtained with different RVEs are limited, indicating that the influence of the number of voxels per grain is limited in this particular case, in agreement with the results in Fernández et al. (2011). This is a particular result for this material because of the strong basal texture. Most of the grains present a similar orientation of the *c* axis (along ND) and there are no important changes in stiffness between neighbor grains. Thus, the strain microfields did not present strong discontinuities across the grain boundaries and the stiffening associated with the poor representation of the strain gradients when the grains are modeled with 1 finite element does not play an important role (Segurado and LLorca, 2013; Zhao et al., 2007). This might not be the case, however, in polycrystals with different texture or deformation mechanisms. Nevertheless, it is important to notice that the hierarchical procedure to start the optimization process with the simplest RVE was very efficient in this case because it was possible to obtain a set of properties very close to the optimum one with little computational cost. Only a few final iterations had to be carried out with the larger RVEs to refine the results.

The results in Table 3 are in agreement with the general observations of the activation of systems in randomly-oriented polycrystalline Mg alloys (including AZ31). Basal slip and tension twinning are the softer deformation mechanisms at room temperature and quasi-static strain rates, while pyramidal and prismatic slip were found to take place at much higher stresses (Barnett et al., 2006; Hutchinson and Barnett, 2010).

The accuracy of the optimization process is clearly shown in Fig. 8(a), in which the experimental and computed stress–strain curves are very close for the three orientations in the whole deformation range. It is worth noting that this excellent agreement is only possible because the physical mechanisms of plastic deformation and the most important microstructural details are incorporated in the computational model. In order to validate the optimization procedure, the tensile test in the RD-ND plane at 45° from both orientations was simulated using the single crystal parameters obtained by optimization and the RVE containing 584 grains. The numerical and experimental stress - strain curves are plotted in Fig. 8(b).The agreement between both is very good and the average error per point similar to the one obtained for the fitted results in the tensile ND tests (Fig. 8(a)).

The set of parameters obtained by the optimization procedure using three independent stress–strain curves as input (Table 3) can be compared with previous data in the literature for rolled AZ31 Mg alloys. Our optimization strategy

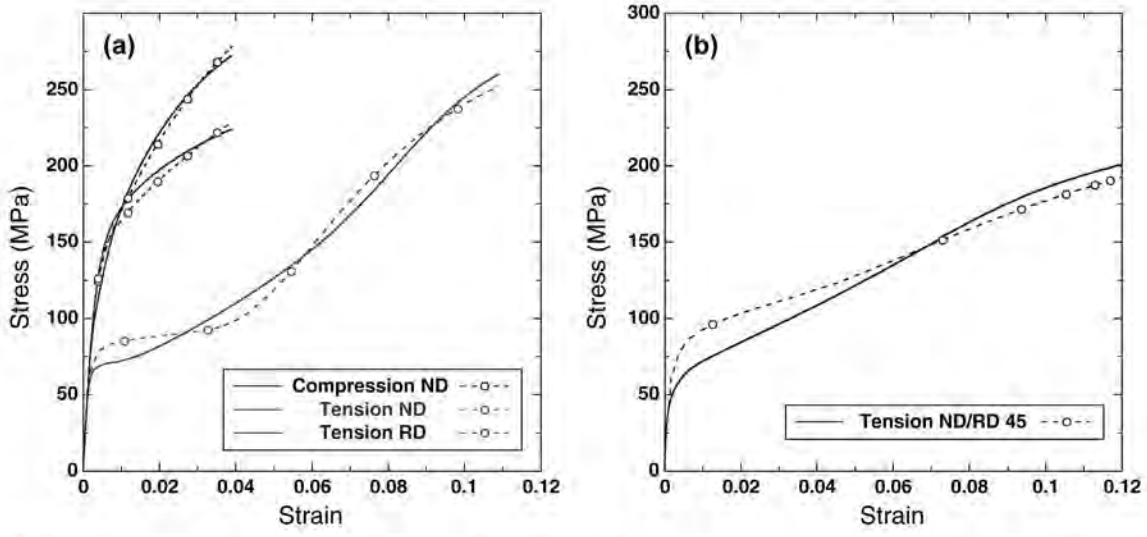

Fig. 8. Results of the inverse optimization procedure using three stress–strain curves (compression ND, tension ND and tension RD) as input. (a) Experimental (solid lines) and numerical (broken lines with symbol) stress–strain curves resulting from the optimization procedure. The numerical results correspond to the RVE with 584 crystals and ≈7 elements per crystal. (b) Model prediction of the tensile test in the RD–ND plane at 45° from both orientations. Solid lines correspond to experimental results while broken lines with symbols stand for the numerical simulations.

provides an initial CRSS for basal slip (23 MPa) slightly lower than that for extension twinning (35 MPa), within the range of most of the studies in the literature. Most investigations concluded than the CRSS for extension twinning was approximately twice that for basal slip (Fernández et al., 2011; Knezavic et al., 2010; Wang et al., 2010), while others predicted that the CRSS for extension twinning was significantly lower (30% to 50%) than that for basal slip (Pei et al., 2011; Agnew et al., 2001). Factors such as alloy composition, processing route and grain size may account for some differences but cannot explain these large discrepancies, which should be attributed to two factors. Firstly, the parameter identification process may not reach the optimum solution if it is carried out manually, by a trial-and-error approach, due to the large number of parameters and the non-linear nature of the phenomenon. Secondly, only two experimental curves are often used to carry out the optimization (Fernández et al., 2011; Wang et al., 2010; Agnew et al., 2001), which correspond to tension or compression tests along RD or ND. If only two tests are considered in the optimization process, it might be possible to identify a set of parameters that provide a reasonable fit to these stress–strain curves, but that are far from the optimum solution.

This latter issue can be checked if only two experimental stress–strain curves are used as input for the parameter identification. In order to check the influence of the particular election of the two stress–strain curves, two different set of simulations have been considered. The first one used as the tests in tension and compression along ND as input for the optimization procedure (ND-T,ND-C) while the second one was based on the tensile tests along ND and RD (ND-T,RD-T). An initial optimization was carried out using the smallest RVE (64 grains and 1 voxel per grain) and the parameters coming from this process were used to predict the tensile test in the RD-ND plane at 45° using the same RVE. The results obtained with the parameters coming from the second data set (ND-T,RD-T) provided a much more accurate prediction, and this indicates that the particular election of the input curves plays a very important role in the optimization procedure.

Starting from the best results obtained with two stress–strain curves as input (ND-T and RD-T), the optimization procedure was completed using different RVEs up to the largest one containing 584 grains and ≈ 7 voxels per grain. The experimental stress–strain curves corresponding to the two directions used for the optimization procedure are plotted in Fig. 9(a) together with the results of the polycrystalline models after optimization. The predictions of the other two independent tests are represented in Fig. 9(b). If the results in Fig. 9(b) are compared with those in Fig. 8(b), it is evident that the predictions of the tensile test in the RD-ND plane at 45° from both orientations are more accurate if three stress–strain curves are used as input instead of only two. A more objective quantitative comparison can be based on the errors (the value of the objective function, Eq. 24, divided by the number of points n in the data set) in the prediction of tensile stress–strain curve in the RD-ND plane at 45° from both orientations. They were 25 MPa/point and 11 MPa/point for the optimizations based on two and three stress–strain curves, respectively. Thus, the inclusion of a third, independent, stress–strain curve as input in the optimization procedure is very important to enhance the accuracy of the predictions for different loading conditions.

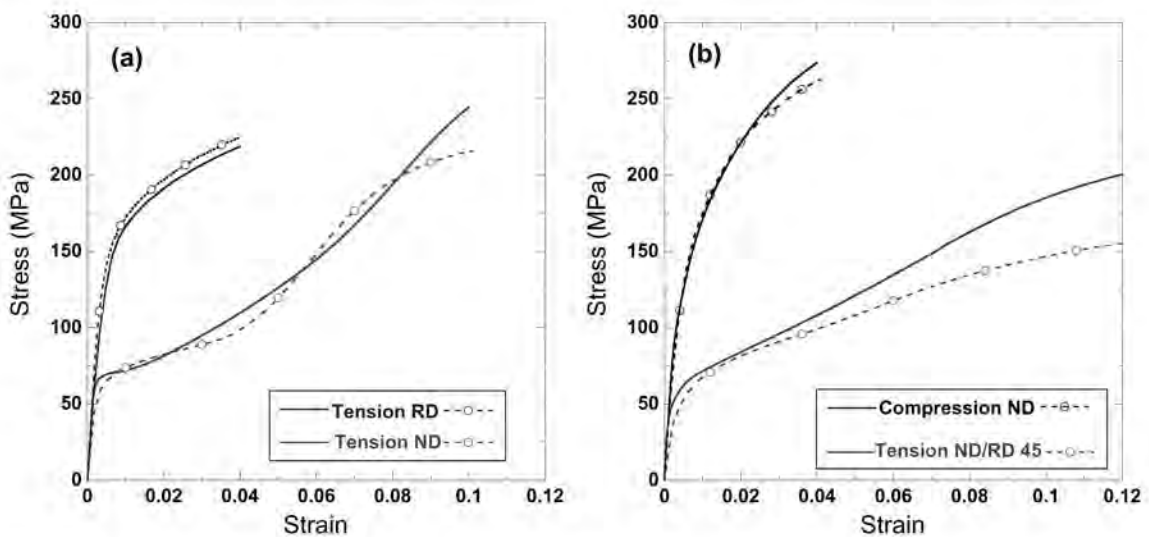

Fig. 9. Results of the inverse optimization procedure using two stress–strain curves (tension ND and tension RD) as input. (a) Experimental (solid lines) and numerical (broken lines with symbol) stress–strain curves resulting from the optimization procedure. The numerical results correspond to the RVE with 584 crystals and ≈7 elements per crystal. (b) Model predictions of the compression test along ND and of the tensile test in the RD-ND plane at 45° from both orientations. Solid lines correspond to experimental results while broken lines with symbols stand for the numerical simulations.

5. Conclusions

An inverse optimization strategy was developed to determine the single crystal properties from the experimental results of the mechanical behavior of polycrystals. The polycrystal behavior was obtained by means of the finite element simulation of an RVE of the microstructure in which the dominant slip and twinning systems were included in the constitutive equation of each grain. The inverse problem was solved by means of the Levenberg–Marquardt method. The methodology was robust, leading to a very good fit of the experimental stress–strain curves. The iterative optimization process began using a simple RVE in which each grain is represented by one voxel and changed to more complex and realistic RVEs once the optimization algorithm has reached the optimum solution for this RVE. This hierarchical approximation was shown to be very efficient from the computational viewpoint.

The optimization strategy was applied to a rolled polycrystalline AZ31 Mg alloy, showing a marked basal texture. The experimental stress–strain curves (corresponding to uniaxial compression and tension along ND and uniaxial tension along RD) were used as input. The values of the initial CRSS, saturation CRSS and initial hardening modulus for basal, prismatic and pyramidal slip and extension twinning, resulting from the optimization process, provided a very accurate fit to the experimental data and were in general agreement with most of the data previously reported for this material. It was shown that this set of parameters was able to accurately predict the stress–strain behavior of the polycrystal along different orientations (tension in the RD-ND plane at 45° from both orientations). Moreover, it was also found that if only two stress–strain curves were used as input in the optimization procedure, the parameters obtained from optimization were not able to accurately predict the mechanical behavior of the polycrystal under different loading conditions. Thus, a minimum of three independent stress–strain curves was necessary to determine the single crystal behavior from polycrystal tests in the case of highly textured Mg alloys.

Acknowledgments

This investigation was supported by the Spanish Ministry of Economy and Competitiveness (project PRI-PIBUS-2011-990) through the Materials World Network program. Ebubekir Dohan and Ibrahim Karaman acknowledge the financial support by NPRP Grant No. 4-1411-2-555 from Qatar National Research Fund (a member of Qatar Foundation).

References

Abaqus, 2013. Analysis User's Manual, version 6.13, Dassault Systemes.
Agnew, S.R., Yoo, M.H., Tomé, C.N., 2001. Application of texture simulation to understanding mechanical behavior of Mg and solid solution alloy containing Li or Y. Acta Mater. 49, 4277–4289.
Anand, L., 2004. Single-crystal elasto-viscoplasticity: application to texture evolution in polycrystalline metals at large strains. Comput. Methods Appl. Mech. Eng. 193, 5359–5383.
Arsenlis, A., Parks, D., 2002. Modeling the evolution of crystallographic dislocation density in crystal plasticity. J. Mech. Phys. Solids 50 (9), 1979–2009.
Asaro, R., Needleman, A., 1985. Overview no. 42 texture development and strain hardening in rate dependent polycrystals. Acta Metall. 33 (6), 923–953.
Barnett, M.R., Keshavarz, Z., Ma, X., 2006. A semianalytical sachs model for the flow stress of a magnesium alloy. Metall. Mater. Trans. A 37A, 2283–2293.
Barton, N.R., Arsenlis, A., Marian, J., 2013. A polycrystal plasticity model of strain localization in irradiated iron. J. Mech. Phys. Solids 61, 341–351.
Bassani, J., Wu, T., 1991. Latent hardening in single crystals. II. Analytical characterization and predictions. Proc. R. Soc. Lond. A 435, 2141.
Bui, Q.H., Pham, X.T., Fafard, M., 2013. Modelling of microstructure effects on the mechanical behavior of aluminium tubes drawn with different reduction areas. Int. J. Plast. 50, 127–145.
Capolungo, L., Beyerlein, I.J., Tom, C.N., 2009. Slip-assisted twin growth in hexagonal close-packed metals. Scr. Mater. 60, 32–35.
Cheong, K.-S., Busso, E., 2004. Discrete dislocation density modelling of single phase fcc polycrystal aggregates. Acta Mater. 52 (19), 5665–5675.
de-Carvalho, R., Valente, R.A.F., Andrade-Campos, A., 2011. Optimization strategies for non-linear material parameters identification in metal forming problems. Comput. Struct. 89, 246–255.
Dennis, J.E., Schnabel, R., 1966. Numerical Methods for Unconstrained Optimization and Nonlinear Equations. SIAM, Prentice Hall, Englewood Cliffs, NJ.
Dogan, E., Karaman, I., Foley, D., Hartwig, K., 2013. Texture modification and microstructural design of AZ31 Mg alloy plate for better formability, Magnesium Workshop Madrid, 2013.
Dream.3d, 2012. Website. <http://dream3d.bluequartz.net>.
Eidel, B., 2011. Crystal plasticity finite-element analysis versus experimental results of pyramidal indentation into fcc single crystal. Acta Mater. 59 (4), 1761–1771.
Evrard, P., Alvarez-Armas, I., Aubin, V., Degallaix, S., 2010. Polycrystalline modeling of the cyclic hardening/softening behavior of an austenitic–ferritic stainless steel. Mech. Mater. 42 (4), 395–404.
Fernández, A., Pérez-Prado, M.T., Wei, Y., Jerusalem, A., 2011. Continuum modeling of the response of a Mg alloy AZ31 rolled sheet during uniaxial deformation. Int. J. Plast. 27, 1739–1757.
Fernández, A., Jérusalem, A., Gutiérrez-Urrutia, I., Pérez-Prado, M., 2013. Three-dimensional investigation of the grain boundary-twin interactions in a Mg AZ31 alloy by electron backscatter diffraction and continuum modeling. Acta Mater. 61, 7679–7692.
Gianola, D., Eberl, C., 2009. Micro- and nanoscale tensile testing of materials. JOM 61 (3), 24–35.
Hill, R., 1966. Generalized constitutive relations for incremental deformation of metal crystals by multislip. J. Mech. Phys. Solids 14 (2), 95–102.
Hill, R., Rice, J., 1972. Constitutive analysis of elastic-plastic crystals at arbitrary strain. J. Mech. Phys. Solids 20 (6), 401–413.
Hutchinson, J., 1976. Bounds and self-consistent estimates for creep of polycrystalline materials. Proc. R. Soc. Lond. A 348, 101–127.
Hutchinson, W.B., Barnett, M.R., 2010. Effective values of critical resolved shear stress for slip in polycrystalline magnesium and other HCP metals. Scr. Mater. 63, 737–740.
Kalidindi, S.R., 1998. Incorporation of deformation twinning in crystal plasticity models. J. Mech. Phys. Solids 46, 267–271 (and 273–290).
Knezavic, M., Levinson, A., Harris, R., Mishra, R.J., Doherty, R.D., Kalidindi, S.R., 2010. Deformation twinning in AZ31: influence on strain hardening and texture evolution. Acta Mater. 58, 6230–6242.
Kothary, M., Anand, L., 1998. Elasto-viscoplastic constitutive equations for polycrystalline metals: application to tantalum. J. Mech. Phys. Solids 46 (51–67), 69–83.

Lebensohn, R., Tomé, C., 1993. A self-consistent anisotropic approach for the simulation of plastic deformation and texture development of polycrystals: application to zirconium alloys. Acta Metall. Mater. 41 (9), 2611–2624.
Lee, E., Liu, D., 1967. Finite-strain elastic–plastic theory with application to plane-wave analysis. J. Appl. Phys. 38 (1), 19–27.
Levenberg, K., 1944. A method for the solution of certain non-linear problems in least squares. Q. Appl. Math. 2, 164–168.
Leyson, G., Curtin, W., Hector, L., Woodward, C., 2010. Quantitative prediction of solute strengthening in aluminium alloys. Nat. Mater. 9 (9), 750–755.
Liu, Y., Wang, B., Yoshino, M., Roy, S., Lu, H., Komanduri, R., 2005. Combined numerical simulation and nanoindentation for determining mechanical properties of single crystal copper at mesoscale. J. Mech. Phys. Solids 53 (12), 2718–2741.
Ludwig, W., King, A., Reischig, P., Herbig, M., Lauridsen, E.M., Schmidt, S., Proudhon, H., Forest, S., Cloetens, P., Rolland du Roscoat, S., Buffière, J.Y., Marrow, T.J., Poulsen, H.F., 2009. New opportunities for 3D materials science of polycrystalline materials at the micrometre lengthscale by combined use of X-ray diffraction and X-ray imaging. Mater. Sci. Eng. A524, 69–76.
Ma, A., Roters, F., Raabe, D., 2006. A dislocation density based constitutive model for crystal plasticity fem including geometrically necessary dislocations. Acta Mater. 54 (8), 2169–2179.
Marquardt, D., 1963. An algorithm for least-squares estimation of nonlinear parameters. SIAM J. Appl. Math. 11, 431–441.
Miehe, C., Schröder, J., Schotte, J., 1999. Computational homogenization analysis in finite plasticity simulation of texture development in polycrystalline materials. Comput. Methods Appl. Mech. Eng. 171 (3–4), 387–418.
Miehe, C., Schotte, J., Lambrecht, M., 2002. Homogenization of inelastic solid materials at finite strains based on incremental minimization principles. Application to the texture analysis of polycrystals. J. Mech. Phys. Solids 50 (10), 2123–2167.
Pei, L., Yun-Chang, X., Qing, L., 2011. Plastic anisotropy and fracture behaviour of AZ31 magnesium alloy. Trans. Nonferrous Met. Soc. China 21, 880–884.
Rice, J., 1971. Inelastic constitutive relations for solids: an internal-variable theory and its application to metal plasticity. J. Mech. Phys. Solids 19 (6), 433–455.
Robertson, I.M., Schuh, C.A., Vetrano, J.S., Browning, N.D., Field, D.P., Jensen, D.J., Miller, M.K., Baker, I., Dunand, D.C., Dunin-Borkowski, R., Kabius, B., Lozano-Perez, T.K.T.S., Misra, A., Rohrer, G.S., Rollett, A.D., Taheri, M.L., Thompson, G.B., Uchic, M., Wang, X.L., Was, G., 2011. Towards an integrated materials characterization toolbox. J. Mater. Res. 26, 1341–1383.
Roters, F., Eisenlohr, P., Hantcherli, L., Tjahjanto, D.D., Bieler, T.R., Raabe, D., 2010. Overview of constitutive laws, kinematics, homogenization and multiscale methods in crystal plasticity finite-element modeling: theory, experiments, applications. Acta Mater. 58, 1152–1211.
Sawaf, B., Ozisik, M.N., Jarny, Y., 1995. An inverse analysis to estimate linearly temperature dependent thermal conductivity components and heat capacity of an orthotropic medium. Int. J. Heat Mass Transfer 38 (16), 3005–3010.
Segurado, J., LLorca, J., 2002. A numerical approximation to the elastic properties of sphere-reinforced composites. J. Mech. Phys. Solids 50, 2107–2121.
Segurado, J., LLorca, J., 2013. Simulation of the deformation of polycrystalline nanostructured Ti by computational homogenization. Comput. Mater. Sci. 76, 3–11.
Segurado, J., Lebensohn, R., Llorca, J., Tomé, C., 2012. Multiscale modeling of plasticity based on embedding the viscoplastic self-consistent formulation in implicit finite elements. Int. J. Plast. 28 (1), 124–140.
Shterenlikht, A., Alexander, N.A., 2012. Levenberg–Marquardt vs Powell's dogleg method for Gurson–Tvergaard–Needleman plasticity model. Comput. Methods Appl. Mech. Eng. 237–240, 1–9.
Sket, F., Enfedaque, A., Alton, C., González, C., Molina-Aldareguía, J.M., LLorca, J., 2014. Automatic quantification of matrix cracking and fiber rotation by x-ray computed tomography during shear deformation of carbon fiber-reinforced laminates. Compos. Sci. Technol. 90, 129–138.
Staroselsky, A., 1998. Crystal Plasticity Due to Slip and Twinning (Ph.D. thesis). Massachusetts Institute of Technology.
Taylor, G., 1938. Plastic strain in metals. J. Inst. Metals 62, 307.
Tomé, C.N., Maudlin, P.J., Lebensohn, R.A., Kaschner, G.C., 2001. Mechanical response of zirconium: I. Derivation of a polycrystal constitutive law and finite element analysis. Acta Mater. 49, 3085–3096.
Tomé, C.N., Lebensohn, R.A., Necker, C.T., 2002. Orientation correlations and anisotropy of recrystallized aluminum. Metall. Mater. Trans. 33A, 2635–2648.
Wang, H., Raeisinia, B., Wu, P.D., Agnew, S.R., Tomé, C.N., 2010. Evaluation of self-consistent polycrystal plasticity models for magnesium alloy AZ31B sheet. Int. J. Solids Struct. 47, 2905–2917.
Zhang, J., Joshi, S.P., 2012. Phenomenological crystal plasticity modeling an detailed micromechanical investigations of pure magnesium. J. Mech. Phys. Solids 60, 945–972.
Zhao, Z., Kuchnicki, S., Radovitzky, R., Cuitiño, A., 2007. Influence of in-grain mesh resolution on the prediction of deformation textures in fcc polycrystals by crystal plasticity FEM. Acta Mater. 55, 2361–2373.